We are IntechOpen, the world's leading publisher of Open Access books Built by scientists, for scientists

5,300
Open access books available

130,000
International authors and editors

155M
Downloads

Our authors are among the

154
Countries delivered to

TOP 1%
most cited scientists

12.2%
Contributors from top 500 universities

CLARIVATE ANALYTICS BOOK CITATION INDEX INDEXED

WEB OF SCIENCE™

Selection of our books indexed in the Book Citation Index in Web of Science™ Core Collection (BKCI)

Interested in publishing with us?
Contact book.department@intechopen.com

Numbers displayed above are based on latest data collected.
For more information visit www.intechopen.com

13

Passive devices for UWB systems

Fermín Mira[1], Antonio Mollfulleda[3], Pavel Miškovský[1],
Jordi Mateu[1,2] and José M. González-Arbesú[2]
[1]*Centre Tecnològic de Telecomunicacions de Catalunya*
[2]*Universitat Politècnica de Catalunya*
[3]*Gigle Networks*
Spain

1. Introduction

The release from the U.S. Federal Communication Commission (FCC) of the unlicensed use of the Ultra-Wide-Band (UWB) frequency range of 3.1-10.6 GHz, fed the interest for developing communication systems to be used on applications requiring high data rate transmission. The complete success and spreading of these novel applications requires inexpensive and reliable UWB communication systems and devices. The set of passive components included in these systems is definitely a key point on their full development. To this end, many efforts have been done by both the academic and industrial sectors, focusing their research activities on the development of UWB passive components. Although the design of passive components for microwave narrow band applications follows well-established procedures or even mathematical description, the development and design of UWB passive components is a challenge, and most of the procedures used on the synthesis of narrow band component, circuit models and design procedures are not applicable for such wideband frequency ranges. In this book chapter we present the design, fabrication and measurement of most of the key passive components playing a role on an UWB communication system. To illustrate so, the following figures, Fig.1a and Fig.1b, outline the transmitter and receiver architecture of the constructed demonstrator at CTTC (Mollfulleda et al., 2006). Although we will not go into details on the design of the whole transmitter and receiver it would allow us to identify the passive components and their role and requirements from a system perspective.
In both, transmitter and receiver architectures we identify as a first and second component of the system chain an antenna and an UWB frontend preselected filter (Mira et al., 2009). The following passive component is a power combiner/splitter for the transmitter/receiver, respectively. The transmitter side also includes a pulse shaping network in the pulse generator box (see Fig.1a) and a pulse inverter necessary in certain modulation schemes. Finally as can be seen in the receiver outlined in Fig. 1b a filter bank will be used on the signal detection.

2. Antennas for Optimum UWB System Performance

According to the definition of the FCC (FCC, 2002) an "UWB antenna" is an antenna that potentially uses all its bandwidth all the time, and its properties are stable across the operational band: impedance match, radiation pattern, gain, polarization, etc. Several types of UWB antennas have thoroughly been described in literature. Generally they have smooth shapes such

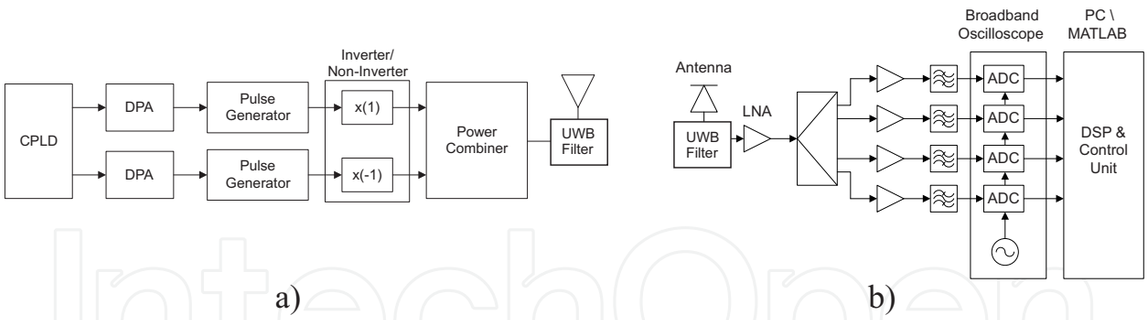

Fig. 1. Outline of the transmitter a) and the receiver b).

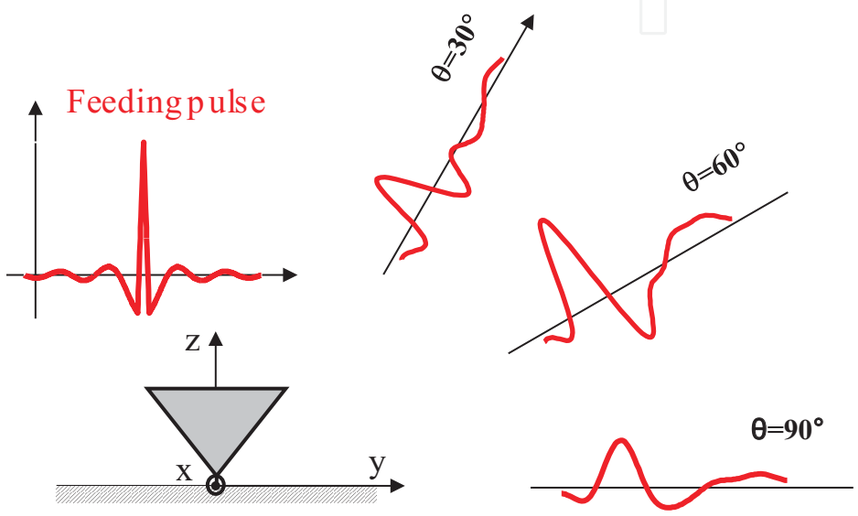

Fig. 2. Spatially dependent distortion of the UWB pulse radiated by triangular UWB monopole.

as the Lindeblad's coaxial horn (Lindeblad, 1941), Kraus "volcano smoke" antenna (Paulsen et al., 2003) or Barnes UWB slot antenna (Barnes, 2000). Usually their performance is assessed in terms of input impedance Z_{in}, gain G, radiation efficiency, etc, independently. In wide frequency ranges this assessment can be a very laborious process because antenna parameters tend to vary significantly across the operational bandwidth, and for some of the aforementioned parameters even with the spatial direction. Due to the wideband nature of UWB signals, the radiated signal distortion, as illustrated on Fig. 2, is an inherent UWB antenna issue that can deteriorate the overall system performance.

For UWB pulse radiation (Montoya & Smith, 1996), transmitting antennas should ideally have low reflected voltage at the feeding port, they should radiate a waveform similar to the feeding pulse (no distortion) or its derivative (known distortion), but they also should have high radiation efficiency. Various antenna impedance loading schemes that potentially could attain these characteristics have been proposed by different authors. Among others, Wu (Wu & King, 1965) intended to extend the bandwidth of the antenna, Kanda (Kanda, 1978) preserved the radiated pulse shape, Rao (Rao et al., 1969) improved the far-field pattern over a range of frequencies, making them potentially interesting in the context of antenna design for UWB systems. Fig. 3 shows how the losses distributed along the antenna can be used to im-

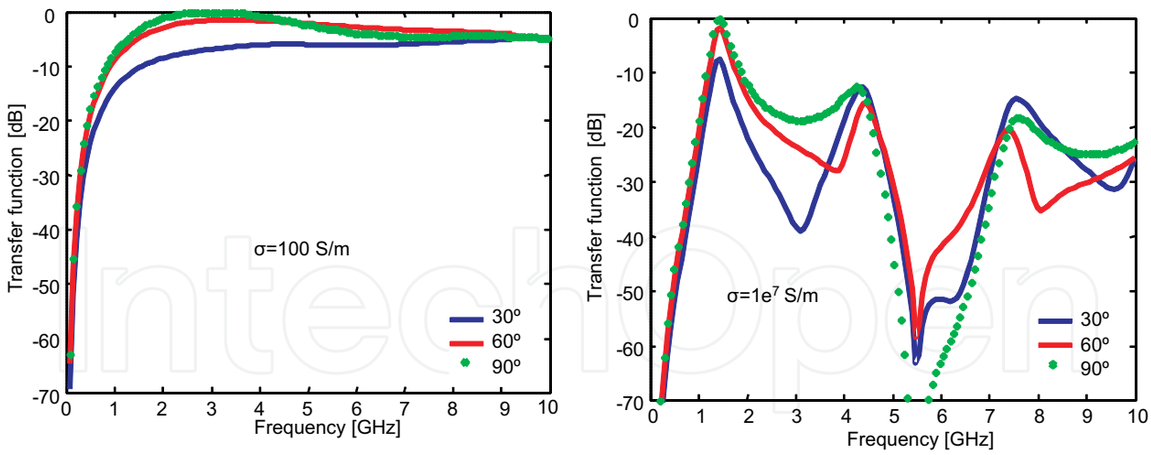

Fig. 3. Transfer functions of a tx-rx system using linear monopoles of different conductivities (left $\sigma = 100$ S/m, right $\sigma = 1e7$ S/m). The receiver antenna is placed in different relative positions $\theta = 30°, 60°, 90°$ with respect to the transmitter. Dotted line represents the spectrum of the transmitter antenna feeding pulse.

prove the antenna performance in terms of radiated pulse distortion. The transfer functions between the transmitter and the receiver load using linear monopoles are shown for two different monopole conductivities. High antenna losses ($\sigma = 100$ S/m) induce less variation in transfer function which is the origin of the low transmitted pulse distortion.
Inspired by the work of Wu, Rao and Kanda, the design of a progressively loaded monopole for an UWB system will be illustrated in the following paragraphs. Specifically resistively loaded monopoles, and to overcome the reduction of radiation efficiency capacitively loaded monopole antennas will be considered. Both types of monopole loadings have been previously reported in the literature (Kanda, 1978), (Rao et al., 1969) and an analytical equation for the loading profiles has been derived in order to achieve a traveling wave (Wu & King, 1965). However in the following paragraphs the design procedure for both types of monopoles uses an evolutionary technique in order to optimize the performance of the monopoles in the sense of radiation efficiency and Spatially Averaged Fidelity (SAF), (Miskovsky et al., 2006), (Miskovsky, 2010). Almost identical figure of merit called Pattern Stability Factor (PSF) was proposed by Dissanayake (Dissanayake & Esselle, 2006).

2.1 Resistively Loaded Monopole

Several optimization techniques can be used to achieve an optimum performance of a resistively loaded monopole in terms of a given set of constraints. Evolutionary techniques, such as genetic algorithms (Johnson & Rahmat-Samii, 1997), particle swarm optimization (Robinson & Rahmat-Samii, 2004) or ant colony optimization (Rajo-Iglesias & Quevedo-Teruel, 2007) are usually used when the degrees of freedom of the problem and the constraints are not connected through equations that allow a gradient optimization. In this particular optimization problem of a resistively loaded monopole a Particle Swarm Optimization technique (PSO) has been used. A wire monopole of height h is considered (Fig. 4a), divided into N segments and having a purely resistive impedance R_i in each segment (being i the segment number). The optimization technique should find the specific set of N resistors to be used along the monopole to achieve both a maximum averaged fidelity SAF and a maximum mean radiation

efficiency e_{rad}. Both constraints are used to define a fitness function F to be maximized by the algorithm, that is:

$$F = \omega_1 \cdot SAF + \omega_2 \cdot e_{rad} \tag{1}$$

In equation (1), ω_1 and ω_2 are weighting coefficients used to stress one of the physical parameters representing the performance of the antenna. In the following explanations SAF and e_{rad} are scaled between 0 and 1 and the coefficients ω_1 and ω_2 are considered equal to 0.5. In order to reduce the time required for the optimization technique to find a solution in the solution space, three considerations have been done:

- To use a commercial set of resistors. This means that a resistor R_i can only take values from a previously selected resistor series (e.g., E12) within the range from 0 Ω to 1 MΩ. A series with a total of 86 resistor values was used.
- To reduce the number of problem unknowns (e.g. problem dimension) instead of solving for a random combination of N resistors. An increasing loading profile is assumed being in accordance with the literature. However some degrees of freedom are added to allow exploring decreasing and decreasing plus increasing profiles. Specifically, the resistive loading profile is considered to follow a parabolic function, quite similar to the one derived by Wu (Wu & King, 1965)

  $$R(z_i) = R_0(z_i - z_0)^2 \tag{2}$$

  the monopole being placed along the z-axis and fed at $z = 0$. Then, R_0 represents the aperture of the parabola, z_0 is the position of the parabola minimum with respect to the origin, and z_i the coordinate center of segment i.
- The tolerance of the resistor values for the chosen resistor series (10%) has not been accounted for.

Such proceeding reduces the number of optimization variables from N (number of resistors) to 2 (number of variables in equation 2). The goal of the optimization is to find the loading profile specified by the values of R_0 and z_0 that maximizes the desired antenna performance objective F. The optimization of the loaded monopole was realized in Matlab® using a method of moments based code named Numerical Electromagnetics Code (NEC) as electromagnetic simulator (Burke & Poggio, 1981). The set of solutions obtained during the optimization procedure (or Pareto front) of 3 monopoles with lengths 11.5 mm, 30 mm and 40 mm and having a radius of 0.8mm is shown in Fig. 4b. The Pareto front shows what performance can be expected from such resistively loaded monopole in terms of radiation efficiency and averaged fidelity SAF. The optimization needed 70 iterations using a swarm of 40 particles. The monopole feeding pulse is considered to have an ideal planar spectrum within the frequency range from 2.5 GHz to 10.5 GHz. As a reference, the unloaded monopoles performance having the same wire radius and lengths should be assessed in terms of fidelity SAF and e_{rad}. In Fig. 4b those can be found on the Pareto fronts as points with the highest possible radiation efficiency. From Pareto fronts shown on Figure 2.4 it can be concluded that by resistively loading a linear monopole there is always a trade-off between the mean radiation efficiency and the spatially averaged fidelity which means that maximum SAF of 1 and maximum mean efficiency of 1 can never be reached simultaneously. The solution having the best fitness F for each monopole is also shown in Fig. 4b.

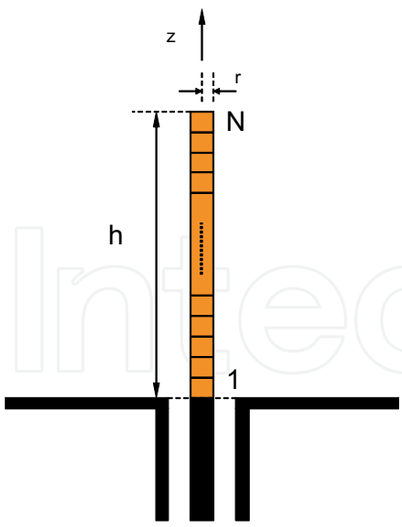

(a) Scheme of the monopole.

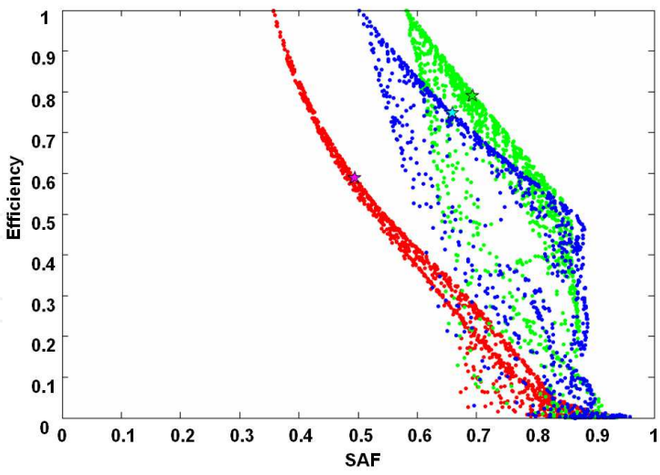

(b) Pareto fronts for three monopole lengths red $h = 11.5$ mm, green $h = 30$ mm, and blue $h = 40$ mm (Miskovsky et al., 2007). Stars represent the solutions with the best fitness for each monopole.

Fig. 4. Monopole with loaded segments.

The overall 3D representation of the radiated pulses at 5.31 m from the 30 mm long monopole (oriented along z-axis) between $\theta = 0°$ and $\theta = 90°$ are shown in Fig. 5. This representation confirms the stable time position of the main peak. The radiated pulses are very similar to the template (ideal pulse feeding the monopole with a planar spectrum in the operating frequency band) for the range $\theta = 60°$ to $\theta = 90°$. However, for the range from $\theta = 10°$ and $\theta = 30°$ the pulse distortion is important compared to the template, but still the major peak position agrees pretty well with the position of the template maximum. The average fidelity SAF is 69%, which means that the transfer function of the obtained antenna is highly wideband. Nevertheless the mean radiation efficiency is 79% which is considerably high value.
The influence of E12 series resistors tolerances was assessed by simulation. The 10% tolerance of resistor value induces a mean radiation efficiency and SAF variation lower than ± 0.5. This is considered acceptable for the monopole fabrication. Unfortunately, the parasitics effects of the discrete component package could influence seriously the monopole performance. Thus for the monopole fabrication some method without the need of considering the parasitics should be used.

2.2 Capacitively Loaded Monopole

To overcome the reduced radiation efficiency of a resistively loaded monopole (due to ohmic losses in the loading resistors) capacitive loading can be used. A capacitively loaded antenna has also been optimized using PSO with the fitness function F defined in terms of SAF and in this case in terms of reflected energy at the feeding point of the antenna. The radiation efficiency was not considered in the optimization because capacitively loaded monopoles are practically 100% radiation efficient. A wire monopole oriented along z-axis with the same physical dimensions as the resistively loaded monopole ($h = 30$ mm, $r = 0,8$ mm) was used as a basic structure. The capacitive loading profile, optimized on such wire monopole follows

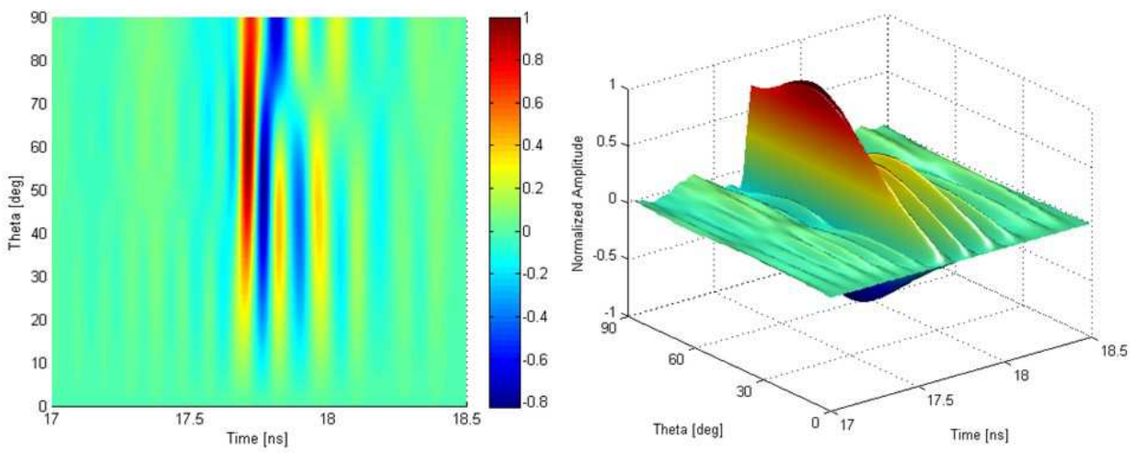

Fig. 5. 3D representation of the pulses radiated by the 30 mm long resistively loaded monopole.

an exponential distribution (3), as defined by Rao (Rao et al., 1969), with capacity decreasing towards the end of the monopole. The capacities are computed for the centers of the monopole segments z_i according to equation (3).

$$C(z_i) = C_0(e^{\alpha z_i} - 1)^{-1} \tag{3}$$

The solution space of the optimization was defined by the parameters that are to be optimized: C_0 and α. The capacity for each segment is chosen from the closest value from *muRata* capacitor kit series, GRM18-KIT-B with values between 0.5 pF and 10 μF . The pulses radiated by the optimized ($C_0 = 1.5e^{-12}$ and $\alpha = 10$) capacitively loaded monopole at 5.31 m and at all angular directions between $\theta = 0^\circ$ and $\theta = 90^\circ$ are shown in Fig. 6. The figure shows that the pulse peak position is stable with direction, and that the pulse shape is quite similar to the pulse fed to the antenna. Fidelity SAF for the best solution is 57% and the reflected energy is 30%. In comparison with the optimized resistively loaded monopole, the amount of reflected energy is practically the same (31% for optimum resistively loaded monopole from previous section). When capacitive loading is used the radiation efficiency is close to 100% within the entire frequency band. The difference in fidelity SAF values is not significant here, due to the different definition of fitness function combining the fidelity SAF with reflected energy instead with radiation efficiency.

2.3 Summary

The radiated signal distortion dependence with spatial direction is an inherent UWB antenna issue, usually assessed qualitatively. Recently proposed compact frequency and direction-independent antenna distortion descriptors such as spatially averaged fidelity can be used to assess the UWB antenna performance in terms of radiated signal distortion. As shown by several authors, the impedance loading distributed along the antenna can be used to improve the antenna distortion performance. Impedance loading of linear monopoles can be optimized by means of antenna descriptors yielding optimum UWB system performance in terms of radiated pulse distortion, radiation efficiency, etc. The evolutionary optimization techniques can

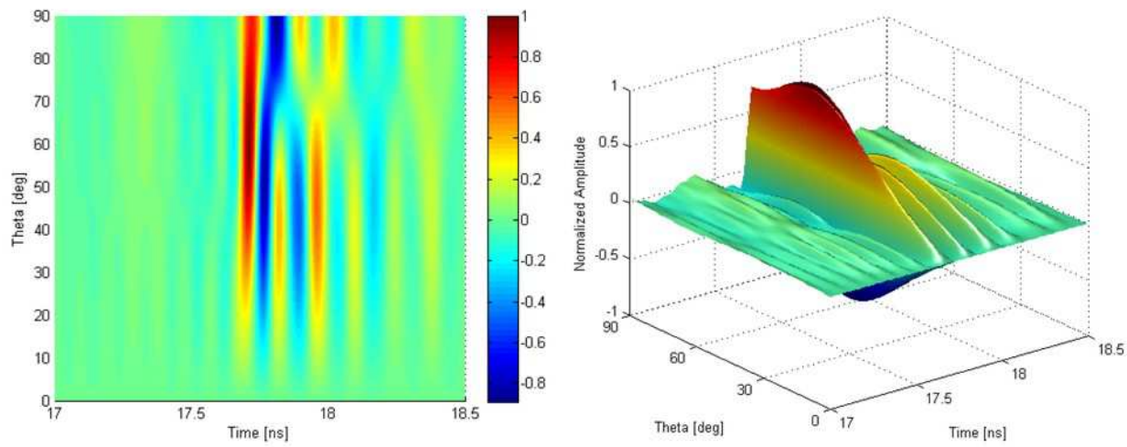

Fig. 6. 3D representation of the pulses radiated by the 30 mm long capacitively loaded monopole.

significantly reduce such optimization problem complexity and consequently the computational load. The performances of the optimum capacitively loaded monopole and optimum resistively loaded monopole of the same length were compared in terms of spatially averaged fidelity, mean radiation efficiency e_{rad} and input port accepted energy. The resistively loaded monopole attains better performance than the monopole with capacitive loading in terms of spatially averaged fidelity, however its radiation efficiency is obviously lower that the efficiency of the capacitive monopole. The performances of both monopoles in terms of the input accepted energy are almost the same. In both cases, the Pareto fronts show what performance can be expected from such loaded monopoles in terms of spatially averaged fidelity, radiation efficiency and amount of energy reflected at the input port.

3. UWB SIW Filter

There is an increasing demand on communication systems which require stringent selective filters with low insertion loss, easy manufacturing and integration into RF circuits. Filters implemented in standard waveguide technology exhibit good performance, but they are bulky, heavy and not suitable for low-cost mass production techniques. On the other hand, microstrip filters present low Q-factors and high radiation losses, especially at millimeter-wave frequencies. Substrate integrated waveguide (SIW) is a recently emerged technology that has attracted much interest because of its low-profile, ease of fabrication with conventional planar circuit processes, such as PCB and LTCC, and achievable high Q-factors. The SIW structure consists of a dielectric substrate comprised between a pair of metal plates which are connected through via holes. This configuration confines the field inside the structure, and therefore does not exhibit undesired couplings between resonators, thus allowing a fine control of the couplings (Tang et al., 2007).

Filters covering a whole microwave band are frequently required in modern transceivers, such as those used in ultra-wideband (UWB) applications. However, few examples of such filters can be found in SIW technology (Zhang et al., 2005)-(Chen et al., 2007), with typical bandwidths between $10 - 20\%$ and responses without any transmission zero. In (Chuang et al., 2007), a dual-mode SIW filter with a bandwidth of 8.5% and transmission zeros is proposed.

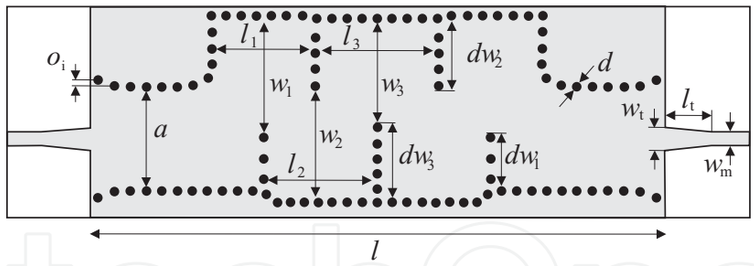

Fig. 7. Design of a seven-pole SIW filter in zigzag meandered topology, where $o_i = 0.9$ mm, $a = 12.80$ mm, $l = 76.62$ mm, $l_1 = 12.74$ mm, $l_2 = 14.11$ mm, $l_3 = 15.40$ mm, $w_1 = 17.23$ mm, $w_2 = 14.43$ mm, $w_3 = 15.64$ mm, $dw_1 = 7.13$ mm, $dw_2 = 9.35$ mm, $dw_3 = 7.76$ mm, $w_t = 2.8$ mm, $l_t = 7.0$ mm, $w_m = 1.85$ mm and $d = 1.05$ mm.

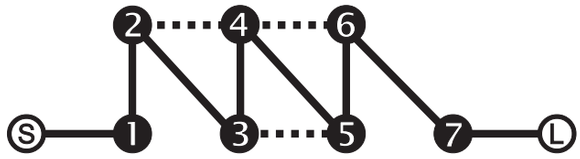

Fig. 8. Coupling topology of the proposed SIW filter.

Bandwidths around 60% are obtained in (Hao et al., 2005) by combining SIW technology with periodic structures.

This section proposes a zigzag filter topology, which includes additional controllable cross-couplings in order to perform sharper responses and a more flexible tuning of the transmission zeros. Therefore, this novel topology has been successfully used for the design of a 28% filter bandwidth for European UWB applications (EU, 2007).

3.1 Design of a SIW Filter in Zigzag Topology

The UWB SIW filter is designed following a zigzag meandered topology (see Fig. 7), originally proposed in (Guglielmi et al., 1995) for waveguide technology. This configuration provides a more compact filter compared to the classical inline topology, and also allows the location of transmission zeros in the upper band due to existing cross couplings between non-adjacent resonators (see the scheme in Fig. 8). These transmission zeros are especially relevant for ultra-wideband applications, since they allow to increase the near upper side out-of-band rejection level of the filter responses. In order to design this novel SIW filter topology, the CAD tool described in (Mira et al., 2007) has been used, since it provides very accurate full-wave responses for SIW filters in CPU times of the order of few seconds.

The SIW filter has been designed using a Rogers RO4003C substrate with thickness 0.813 mm, dielectric constant $\epsilon_r = 3.60$ (the manufacturer recommends $\epsilon_r = 3.55 \pm 0.05$ for circuit design purposes), and loss tangent $\tan\delta = 0.0027$ at 10 GHz. This low-cost substrate, widely employed for manufacturing printed circuits, allows an easy metallization of the vias holes without initial special treatment.

The symmetric configuration shown in Fig. 7 provides a seven-pole electrical response, due to the inner five SIW resonant cavities coupled following a zigzag shape, and to the input and output SIW sections that are connected to the feeding lines through waveguide to microstrip transitions (Deslandes & Wu, 2001). The width a of the input and output sections defines the sharpness at the band-edge in the lower side band, due to the transmission zero introduced by

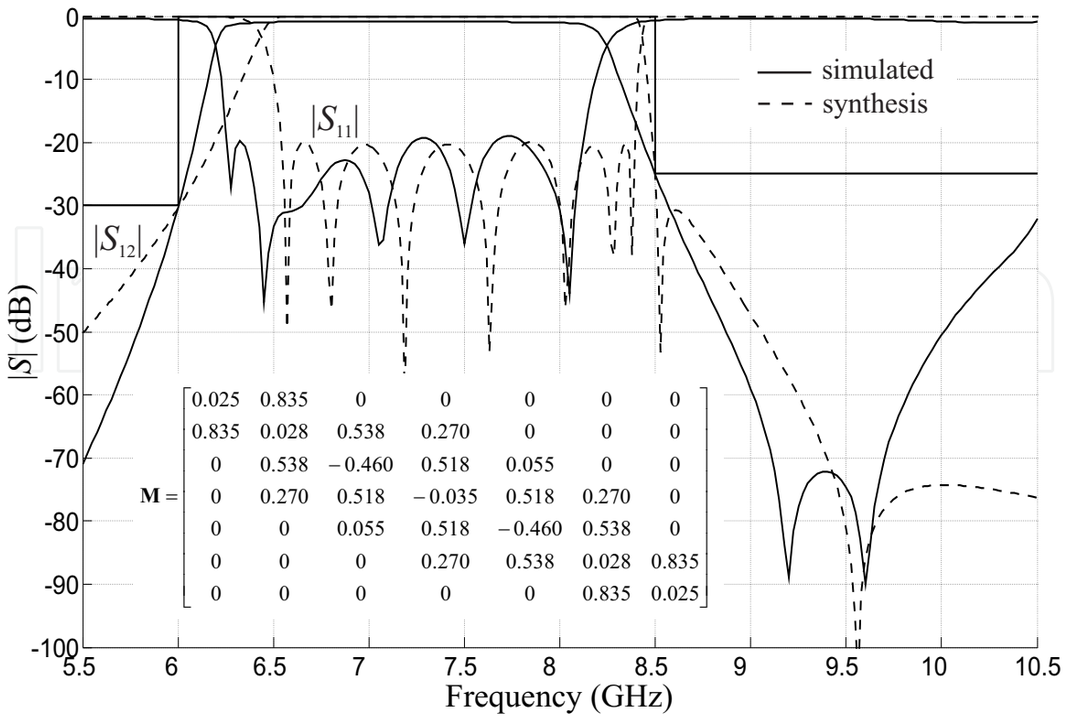

Fig. 9. S-parameters provided by the synthesized coupling matrix related to the scheme in Fig. 8 ($R_S = R_L = 0.9898$), and simulated data for the SIW filter of Fig. 7.

the finite cut-off frequency of the waveguide. Additionally, the parameter o_i is used to adjust the level of the return losses. Finally, each cavity is bounded by decoupling walls dw_i, whose lengths l_i and widths w_i are found to set the resonant frequencies of the cavities and recover the required couplings between them.

The SIW filter has been designed to comply with the European UWB mask, that imposes $|S_{12}| = -30$ dB at 6 GHz and $|S_{12}| = -25$ dB at 8.5 GHz (see Fig. 9). Our aim is to comply with the proposed mask for frequencies up to 10.5 GHz. In Fig. 9, we include the goal synthesized response for the scheme of Fig. 8, considering a bandwidth of 1.84 GHz and two transmission zeros in the upper band for satisfying the restrictive UWB requirements (synthesis). At the same time, we found the dimensions for the initial SIW filter structure of Fig. 7 that best fits the UWB mask, whose response is also included in Fig. 9. As it can be observed, the simulated response of the SIW filter has a return loss level greater than 19 dB (achievable because of the displacement o_i introduced in the first via holes), a very selective upper side of the out-of-band response due to the two synthesized transmission zeros, and a more pronounced fall in the lower side band attributed to the higher cut-off frequency of the input and output sections.

3.2 Introduction of Flexible Cross-couplings

Although the two transmission zeros placed at the upper band edge of the previous filter give rise to an improved selectivity response, its zigzag meandered topology only allows for achieving moderate cross-couplings between non adjacent cavities, and therefore a limited control on the location of the transmission zeros. As it can be observed in the synthesized response of Fig. 9, the filter selectivity can be improved when the first transmission zero is placed closer to the pass-band. For such purpose, it is required to have a higher degree of

control of the cross-couplings, which can be obtained through the opening of the decoupling walls (dw_i with $i = 1, 2, 3$ in Fig. 7) by removing one of the via holes as shown in Fig. 10.
Fig. 11 outlines the effect of opening the decoupling walls dw_1, dw_2, and dw_3, respectively. In doing so, the spacing between transmission zeros and their position can be controlled, pushing the first spurious response toward higher frequencies. In Fig. 11, we see that by opening the first decoupling wall dw_1 the first transmission zeros are brought closer to the band edge, which improves the selectivity and reduces the transmission zero spacings. A similar effect over the selectivity is observed by opening the second decoupling wall dw_2, now increasing the space between the two transmission zeros. Finally, by opening the third decoupling wall, the transmission zero spacing increases and the out of band response improves, although the pass-band is slightly reduced.

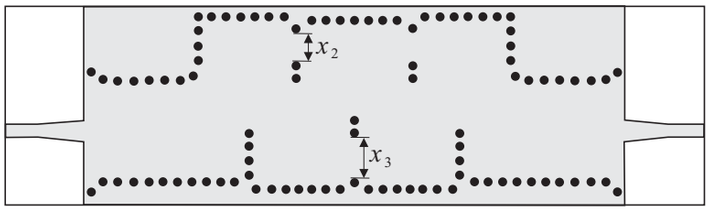

Fig. 10. Design of a seven-pole zigzag SIW filter topology with more flexible cross couplings, where $o_i = 1.3$ mm, $a = 12.79$ mm, $l = 76.62$ mm, $l_1 = 12.33$ mm, $l_2 = 13.35$ mm, $l_3 = 14.90$ mm, $w_1 = 14.89$ mm, $w_2 = 14.09$ mm, $w_3 = 12.61$ mm, $dw_1 = 6.62$ mm, $dw_2 = 8.43$ mm, $dw_3 = 9.41$ mm, $x_2 = 4.02$ mm and $x_3 = 5.76$ mm, $w_t = 2.8$ mm, $l_t = 7.0$ mm, $w_m = 1.85$ mm and $d = 1.05$ mm.

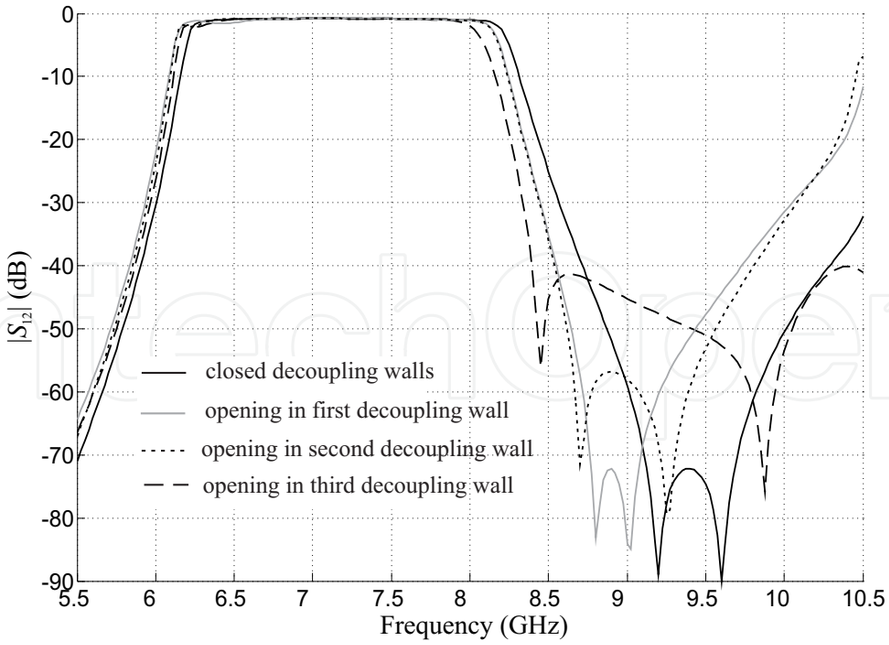

Fig. 11. S-parameters of the novel SIW filter topologies.

Thus, making use of the additional degree of flexibility provided by the novel SIW structure shown in Fig. 10, we may obtain the synthesized values of the goal coupling matrix to get a

more selective response (synthesis of Fig. 9). Using this information, a new SIW filter has been designed by opening the second and third decoupling walls. These changes in the filter topology improve the selectivity, and move the first spurious response towards higher frequencies. The layout of this new filter is shown in Fig. 12, and its simulated response is outlined in Fig. 13 with grey solid lines. In the same figure, we also show the simulated response for the first SIW filter displayed in Fig. 7 with grey dashed lines. It can be concluded that the new SIW filter exhibits a better selectivity, due to the proximity of the first transmission zero to the pass-band, while also preserving a good out-of-band performance with $|S_{12}| < -25$ dB from 8.5 GHz to 10.5 GHz.

Finally, two prototypes of the designed filters have been manufactured in order to validate the simulated results. Measurements of the two filters are overlapped with the simulated results in Fig. 13, showing a very good agreement with numerical data and compliance with the UWB proposed mask (EU, 2007). The measurements have been performed by means of a universal test fixture with 1.85 mm connectors. The connectors are not included in the calibration procedure, and the associated insertion losses have been estimated about 0.30 dB. Although both designed and measured filters satisfy the UWB mask, the second one exhibits a better fitting into the mask due to the placement of transmission zeros closer to the band edges. According to the measurements, the transmission response for the first filter falls to -30 dB at 5.9928 GHz and -25 dB at 8.4985 GHz, whereas for the filter with more flexible cross-couplings it falls to -30 dB at 5.9967 GHz and -25 dB at 8.4904 GHz. With regard to the return losses, the first filter has a minimum value of 19 dB, whereas for the second case it slightly decreases to 17 dB.

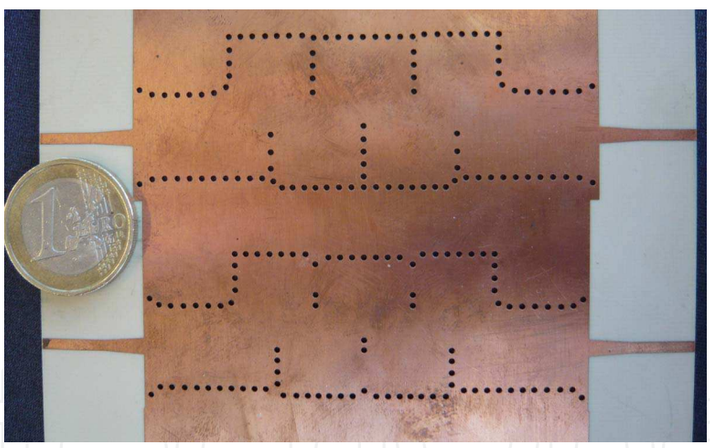

Fig. 12. Layout of the fabricated UWB SIW filters

The insertion losses for the second SIW filter are presented in Fig. 14, where they are compared with the results provided by the commercial software Ansoft HFSS (v.11.1). The simulation data have been obtained by assuming several values for the metal conductivity, which in practice is lower than the nominal one (Tang et al., 2007), (Bozzi et al., 2007). Taking into account that the connector losses are around 0.3 dB, in our case an equivalent conductivity of $\sigma = 1.6 \cdot 10^7$ S/m compares rather well with the experimental results. Removing the connector losses, the complete filter (including the microstrip to SIW transitions) has an insertion loss level of 1.18 dB, which reduces to 1 dB if the transitions are not considered. Such results provides an estimated Q-factor of around 220 for the rectangular SIW resonator at 7.5 GHz.

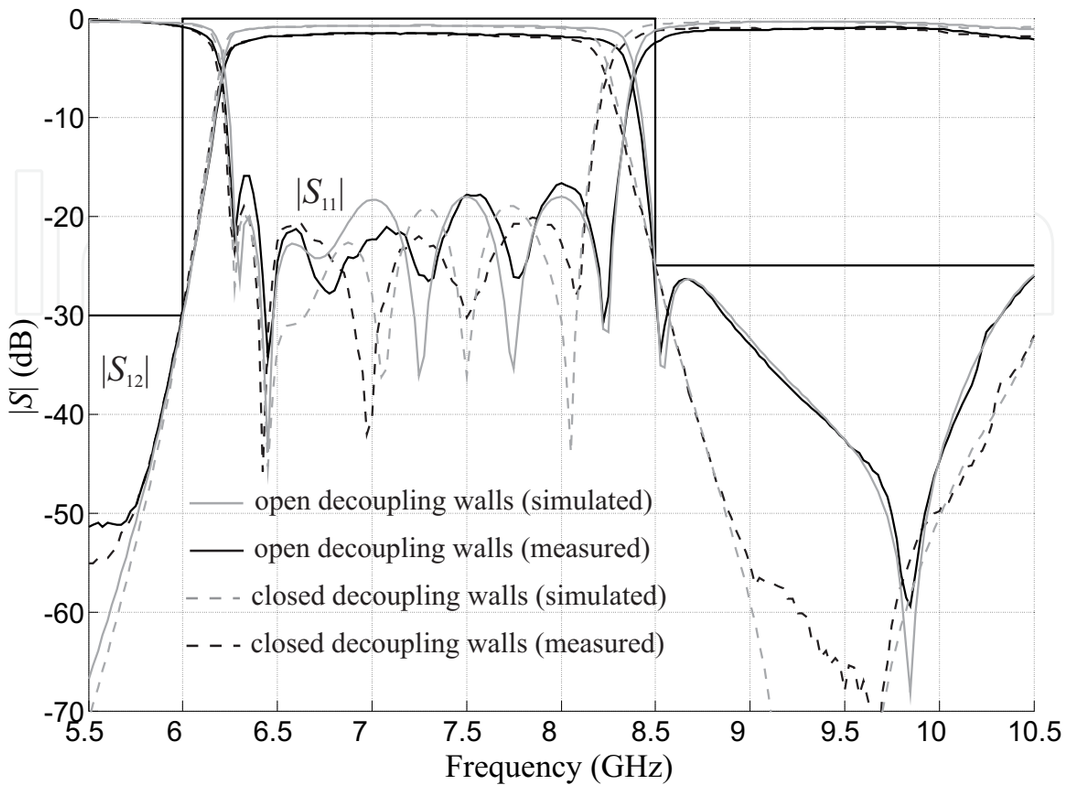

Fig. 13. Comparison between the electrical responses of the two designed and fabricated UWB SIW filters.

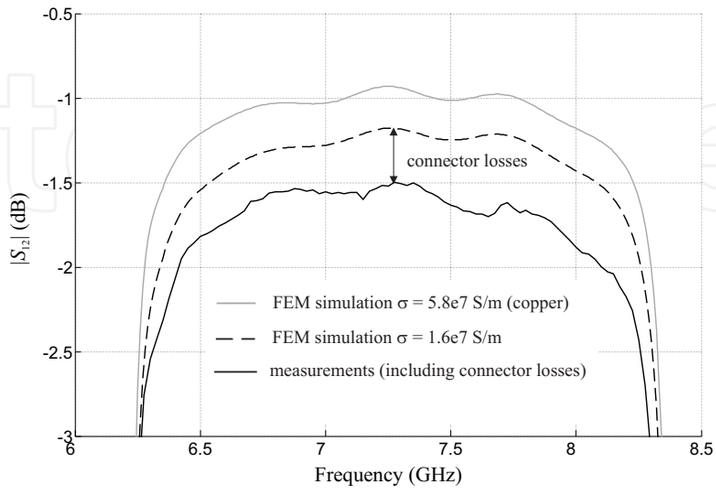

Fig. 14. Insertion losses for the UWB SIW filter shown in Fig. 10 and Fig. 12.

4. Filter Bank for UWB Systems

A microwave filter-bank has been designed for the development of an all-digital Impulse Radio (IR) Ultra-Wide-Band (UWB) receiver. The receiver is based on a frequency domain sampling technique, where each filter precedes one sampling unit, taking the energy for a given frequency band. Therefore, each band is digitalized in a parallel scheme by a set of relaxed sampling speed Analog-to-digital converters (ADC) (see Fig. 1b). Note that its real time sampling scheme counterpart would impose stringent demand on sampling speed, which for FCC compliance would be 20 Gsps, resulting unfeasible for most practical implementations.
To implement an optimal receiver the set of filters requires covering the whole spectrum of the received signal energy in a set of orthogonal frequency bands. The complexity of the receiver is determined by the number sampling units, that is the number of filters, and the sampling rate, which essentially relates with the bandwidth of each filter. A reduced number of filters results in wider bandwidth and larger ADC sampling rates, whereas a large number of filters results in lower ADC sampling rates. Therefore, a tradeoff exists between the number of filters and the sampling rate of the ADCs to be used in the receiver implementation.
The microwave filter bank presented in this work consists of a total of four filters with equal bandwidth in order to cover the frequency range inside the FCC UWB spectrum (3.1GHz - 10.0GHz). This results in four filters 1.57GHz equally spaced in frequency. The bandwidth and shape of the filter frequency responses are essentially related in the way the energy is obtained at each frequency band and therefore determining the signal reconstruction procedure, which is assumed to be implemented on the DSP & Control Unit of Fig. 1b. A set of quasi-orthogonal basis of filter frequency responses and yet capture the whole signal energy, could be performed by means of filters with very sharp selectivity and flat in-band frequency response. This in practice needs of high order filters implemented with very high Q resonators, which might be unfeasible for consumable UWB equipment.
This work bases the signal reconstruction procedure on the frame theory techniques (Daubechies, 1990). This theory essentially provides the mathematical tools for signal reconstruction when the set of frequency samplers (filters) does not constitute an orthogonal set of functions. Note that this is very interesting from a practical point of view, since may account for the technological limitation and even for the manufacturing imperfections of the RF components. From the theory of frames we may conclude that any type of filter could be used for the signal reconstruction (Daubechies, 1990). However it can be also demonstrated that an IR signal a Gaussian like filter type response is the one producing the best mean squared error of the signal reconstruction for a given scheme complexity (Mollfulleda et al., 2010). At this point is also worth to mention that the bandwidth of the Gaussian filter for the signal reconstruction has been defined down to -10dB.
A Gaussian like filter type exhibits a frequency response with no flat in-band performance, rounded band edges and poor selectivity. Note that those characteristics are common in any lossy low order filter (Hong & Lancaster, 2001). Therefore, in addition of synthesizing a Gaussian filter response which would result in an asymmetric topology and an increased the number of couplings to be designed, a Gaussian like response can be implemented by means synthesizing a conventional low order Butterworth or Chebyshev responses, using low Q resonators. We choose to design four Butterworth bandpass filters of order 3. The designing parameters (central frequency F_0, bandwidth B_w and fractional bandwidth FBW) of each filter are detailed in Table 1.
Since the four filters have the same B_w and are centered at different frequencies, the fractional bandwidths ranges from 17.4% to 39.2%. The FBW is a critical parameter on the filter design,

	Filter 1	Filter 2	Filter 3	Filter 4
F_0 (GHz)	4.0	5.6	7.3	9.0
B_w (GHz)	1.57	1.57	1.57	1.57
FBW	39.2%	28.0%	21.4%	17.4%

Table 1. Design parameters the filter-bank.

since it sets the coupling strength between resonators, and may therefore set the technology to be used for the filter implementation as well as the filter topology. For instance, in planar technology, filters with very small fractional bandwidth could be implemented with end coupled resonators, since the coupling between resonators have to be very weak. In contrast, this topology cannot be used for the design of wider band filter and one usually needs to go for parallel coupled resonator configurations (Hong & Lancaster, 2001).

We desired to use the same topology for the design of the four filters. The target is to specify a single filter configuration properly scaled in size in order to be mapped at the corresponding frequency band. In practice this results in filters with the same electrical length which in conjunction with the filter bandwidths (equal for all filters, see Table 1) will give filters with the same group delay. Although this condition is not essential for the signal reconstruction it facilitates the reconstruction procedure.

We used planar technology for the design of the filters and the proposed filter configuration is outlined in Fig. 15. This topology consists on a double-sided configuration to combine microstrip and coplanar resonant modes coupled by means of wideband couplings. The wideband couplings have been performed by elliptical patches, which allow us to control the coupling according to the size of the patch. Fig. 15 shows the top and bottom layers of a single filter. The top layer (Fig. 15a) is formed by the 50Ω feeding lines connected to an elliptic patch. The elliptic patch is then coupled to a resonator in the bottom layer (Fig. 15b).

The resonator in the bottom layer consists on a high impedance resonant transmission line with elliptic patches at both ends. The high impedance transmission line results in a resonator with low Q which helps to round the filter shape on the edges and therefore resembling into a Gaussian filter. The function of the elliptic patches connected at the ends of the resonator is twofold. These elliptic patches help to control the coupling between the resonators and the input/output port as well as between the other resonators. Note that this coupling will be very different depending on the filter designed (filter 1, filter 2, filter 3 or filter 4 of Table 1). The elliptic patches are also loading capacitively the resonator and therefore reducing its physical length for a given resonant frequency (Abbosh, 2007).

The resonator in the bottom layer is then coupled to the resonator at the top layer. The resonator at the top layer consists of a 50Ω resonant transmission line, again capacitively loaded at both end by means of an elliptic patch. As in the resonator in the bottom layer the function of the elliptic patch is to reduce the length on the resonator and to control the coupling between the resonator of the top and bottom layer.

Note that the presented topology is functioning like an end coupled filter where the resonators are conveniently distributed in two layers and the end of the resonators is properly designed to control the wider range of required couplings. Note that if we would instead be used a single layer for the filter designs, the couplings between resonators would required to set the coupling very close, probably resulting in unfeasible for conventional planar technology.

Once decided the filter topology and shape of the resonators to be used, the dimensions of the layout, this is width and length of the transmission lines, and dimensions of the elliptic

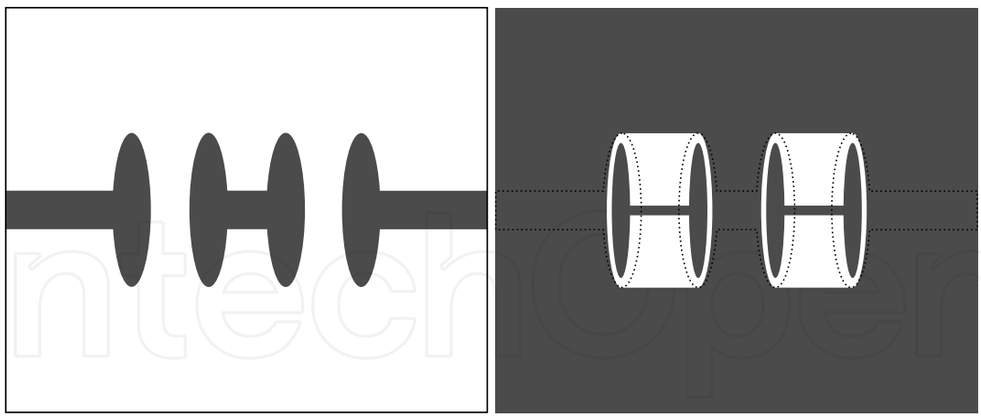

(a) Top layer

(b) Bottom layer. Dotted line is the top layer outline.

Fig. 15. Layout of the designed fitler.

patches, have been designed using conventional techniques for the design of coupled filters (Hong & Lancaster, 2001). The material used for the design of the four filters is Rogers 4003 with 3.38 of dielectric permittivity, the thickness of the dielectric is 0.5 mm and with 17 μm of cooper metallization at both sides. The loss tangent of the dielectric over the whole frequency range is assumed to be constant to 0.002.
Finally the designed filters have been fabricated and measured. In Fig. 16 we show the picture of the bottom and top layer of the filter at lower frequency (Filter 1 of Table 1). Fig. 16 also shows the measured and simulated response of Filter 1, showing both very good agreements over the whole frequency range. Fig. 16 shows the top-view of the whole filter bank, showing the compactness of the filters. Also in Fig. 16 we can see the frequency response of the whole filter bank. The frequency responses cover the whole frequency range and consecutive filter cross-over at the defined bandwidth of -10 dB, as expected from the design.

5. Shaping Networks

The shaping network is a passive component included in the pulse generator device on the transmitter side and it is essentially used to adjust the generated pulse into the UWB mask. In this section we will present two different approaches for the pulse shaping implementation. Both circuit approaches have been designed, fabricated, measured and tested.
The first approach uses the concept of a transmission line connected to a short-circuited stub. The transmission line is then fed by stepped signal, which due to the reflection and sign inversion occurring in the short-circuited stub generates a Gaussian monopulse which spectrum fits the UWB mask. In the proposed topology this idea is implemented by means of a balanced network following a hybrid configuration. This new configuration compensates the unbalanced effects due to the T-junction between the transmission line and the short-circuited stub (Mollfulleda et al., 2005). We refer to this approach as Hybrid configuration.
In contrast with the previous approach, the second one presents a shaping network which needs to be fed by a very narrow impulse whose frequency response it is almost flat in frequency. Then the function of the proposed shaping network is fitting such a response into the UWB mask. To this end we proposed a very compact topology which consist of two coupled

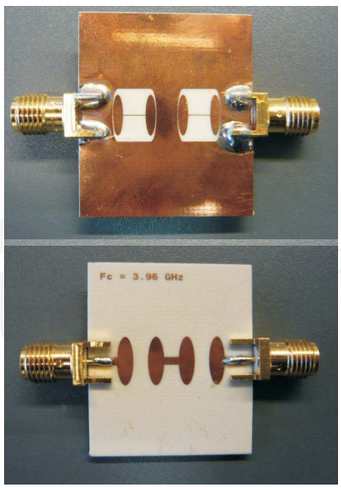

(a) Picture of Filter 1

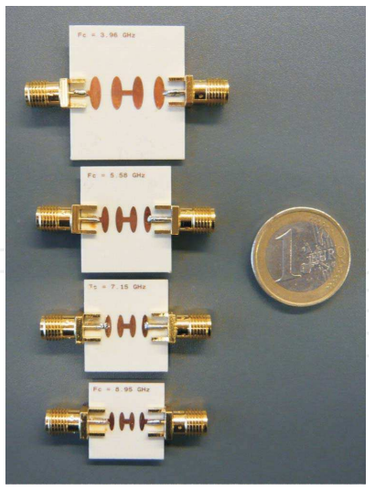

(b) Picture of the filter-bank

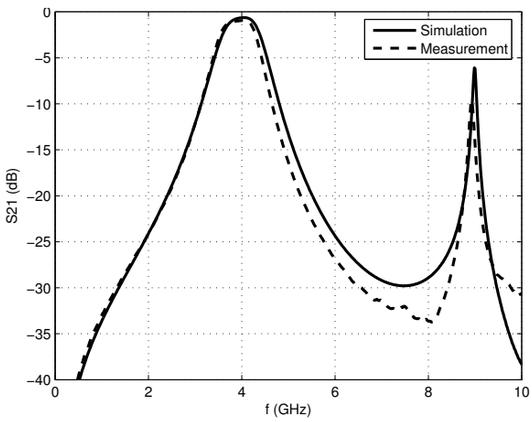

(c) Measured S21 on Filter 1

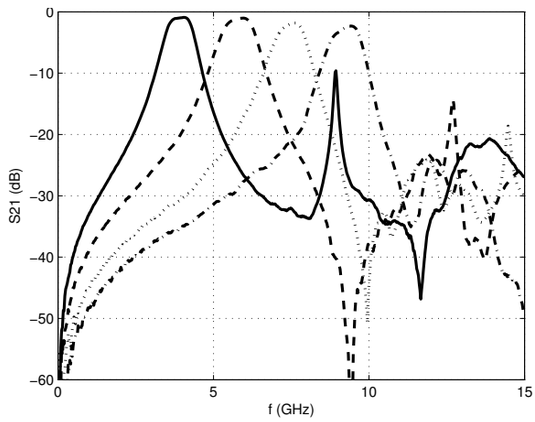

(d) Measured S21 on Filter-bank

Fig. 16. Picture and frequency response of fabricated filter-bank.

lines in the top layer and increases its bandwidth by introducing a coupling slot on the ground plane. We refer to this approach as Coupled line configuration.

5.1 Hybrid Configuration

The concept of a transmission line connected to a short-circuited stub can be illustrated as in Fig. 17, where a Z_0 impedance transmission line is loaded with a $Z_0/2$ impedance short circuit stub. Then the Guassian pulse results from the summation of the travelling wave through the main transmission line and the reflected signal coming from the stub, when an step signal is driven in port 1.

The connection between the transmission line and the stub is typically performed by means of a T-junction. In practice, the T-junction introduces unbalanced response in the rising and falling edge of the output pulse, i.e., the step propagated towards the stub and the step propagated towards the load have different amplitude (Ross, 1965). As a consequence a degraded impulse response is obtained. In other words, when the circuit is fed with and impulse ($\delta(t)$)

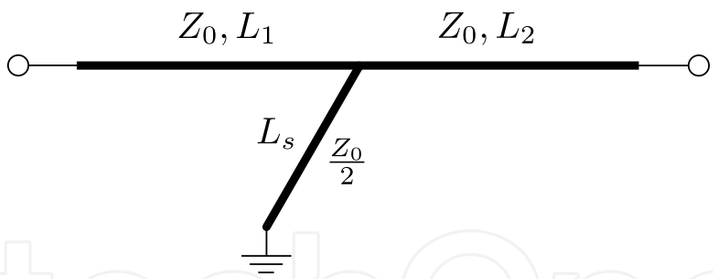

Fig. 17. Single short-circuit stub pulse shaping network.

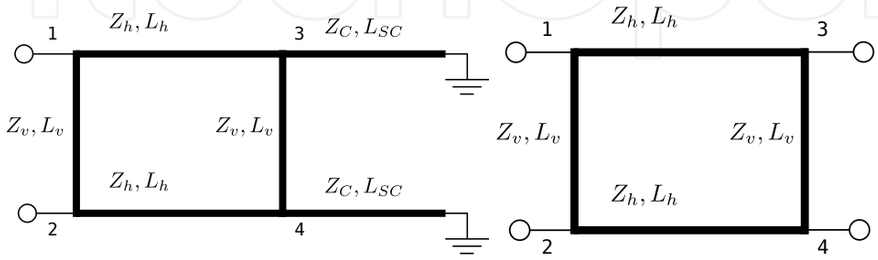

(a) Hybrid shaping network loaded with short-circuited stubs.

(b) unloaded 4-port hybrid symmetric-topology.

Fig. 18. Robust shaping network based on hybrid topology.

the response of the circuit can be written

$$h_{DLSN}(t) = k_1 \delta(t - \tau_1) - k_2 \delta(t - \tau_2) \tag{4}$$

where τ_1 and τ_2 represent the delays of the output impulses and depend on the dimension of network (see L_1, L_2 and L_s of Fig. 17 The scaling factors k_1 and k_2 represent their corresponding amplitudes.

The unbalanced response of the T-junction makes k_1 different than k_2. Ideally, one would like to obtain a balanced response ($k_1 = k_2$). To do that we might tune the impedances of the circuit of Fig. 17, at the expense of introducing further significant delayed versions of the input signal (Smith, 2002).

The work reported in (Mollfulleda et al., 2005) is described, whose network topology is shown in Fig. 18a. The hybrid-symmetric topology of this structure allows to compensate the effects introduced by the T-junction. The values Z_v, Z_h, and L_h, L_v, $L_s c$, are respectively the impedances and length of the corresponding transmission lines.

To analyze the proposed structure, we start considering the 4-port network of Fig. 18b. When the port 1 is excited with an impulse signal $\delta(t)$, it produces a train of impulses at ports 2, 3 and 4. These responses can be expressed as:

$$h_{1i}(t) = k_{1i} \delta(t - \tau_{1i}) + \sum_j k_{ij} \delta\left(t - \tau_{ij}\right) \tag{5}$$

where $h_{1i}(t)$ is the signal at port i, k_{1i} and τ_{1i} are the amplitude and delay of the first signal reaching port i, respectively. k_{ij} and τ_{ij} are the amplitude and delay of the impulses that appears at point i caused by further internal reflections on the structure.

The design of the structure must be performed so as to consider negligible the additional terms in (5). From now on, we will assume that $h_{1i}(t)$ is only composed of the first reaching impulse.
When the ports 3 and 4 are loaded with the short circuit stubs (as shown in Fig. 18a), the corresponding impulses are reflected back signed inverted. By considering the symmetric topology of the network the resulting impulse response results:

$$h_{12} \approx k_+ \delta(t - \tau_{12}) - k_- \delta(t - \tau_{13} - \tau_{14} - \tau_{SC}) \quad (6)$$

$$k_+ = k_{12}, \quad k_- = 2k_{13}k_{14} \quad (7)$$

where τ_{SC} is the one way propagation delay of the short circuit stub. Note that the length of the stubs in ports 3 and 4 may be used to determine the pulse width. However, also note that the minimum pulse width depends on the values of τ_{12}, τ_{14} and τ_{13}, which in turn depend on the dimension of the network (L_v, L_h). Since this topology has more parameters to be adjusted (Z_v, Z_h, L_h, L_v, L_{SC}) it offers a better control on the desired amplitude and delay of the outcoming impulses, i.e, k_+, k_- and τ_{1i} in (6), and even on the amplitude of the undesired delayed versions of the input impulse.
The design process consists of adjusting the parameters Z_v, Z_h, L_h, L_v, L_{SC} to get an impulse response as (4) with $k_1 = k_2 = 0.5$. Given the symmetric topology of the network, it is just required to adjust one of the impedances (Z_v or Z_h) and one of the line lengths (L_h or L_v).
We start the design we start fixing L_v and Z_v. The length L_v determines the signal delay of the shaping network, τ_{12} in (6). For this design we fix $\tau_{12} = 110$ ps. The input and output impedance as well as Z_v have been set to $Z_1 = Z_2 = Z_v = 50\Omega\frac{1}{2}$.
Under the assumptions above, the values of k_+ and k_- in (6) mostly depend on Z_h. In addition the length of the lines is straightly related to the technology and permittivity of the material to be used. In this case we assume microstrip technology with a dielectric constant of 3.
The design process is divided in two steps. In the first step Z_h is set so to achieve $k_+ \approx k_- \approx 0.5$. To do that ports 2, 3 and 4 are loaded to match 50Ω. By simulating the device response we asses k_+ and k_- as a function of the impedance Z_h. Simulation results provide $Z_h = 70.71\Omega$.
The second step takes the simulation model of Fig. 18a and the value of k_- is evaluated as a function of L_h. By simulation we obtain a length $L_h = 2.2$ mm giving a value of $k_- = -0.496$.
To test the procedure described so far we have built and measured an Hybrid-Symmetric pulse shaping circuits. The structure had been implemented in microstrip technology. The substrate had 1.52 mm thickness and a dielectric permittivity of 3. Fig. 19a shows a picture of the design.
The resulting topology had been measured using a E8361A Vector Network Analyzer from Agilent Technologies. This instrument allows to measure the frequency response of the device and to compute its time domain impulse response by means of an inverse Fourier transform. As well-known from signal processing theory, the resolution in the time response is inversely proportional to the window frequency. The result presented below has been obtained with a wide-band measurement up to 30 GHz.
Fig. 19 shows the measured and simulated time response. The simulated performances had been modified to account the delay introduce by the SMA connectors and the out-of-layout commercial short circuit. The results presented at Fig. 19 exhibit a very symmetric response, i.e. k_+ and k_- in (6) are nearly equal. As expected from the analysis above, this circuit configuration compensates the effects introduce by the T-junction, so that the two main reflected impulses reach the output port at the same time.

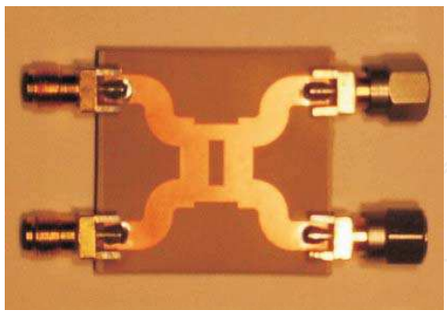

(a) Fabricated shaping network.

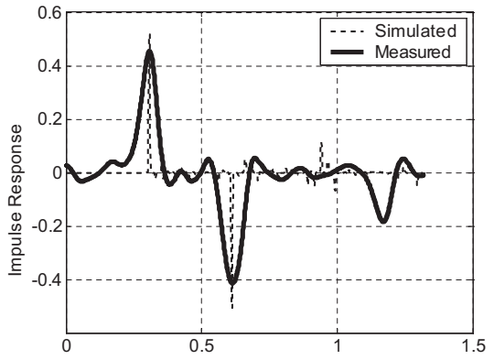

(b) Measured and simulated Results.

Fig. 19. Impulse response of fabricated shaping network.

5.2 Coupled line Configuration

The shaping network topology presented in this section consists on a pair of parallel coupled transmission lines, being the aim of the design to coupled energy only in the band where the UWB is defined. The proposed design uses the idea presented in (Li, 2006)]. Figure 20 outlines the layout of the designed shaping network, where in the top layer it can be identified the input and output 50Ω transmission lines connected to a narrower transmission lines which are coupled to each other. In a conventional coupled transmission line structure the strength of the coupling is essentially set by the proximity between the two transmission lines and the line width (Gupta, 1996). In this case a wideband strong coupling is required to meet the specifications of the UWB system. To achieve so, an slot aperture is introduced in the ground plane of the topology. The layout of the aperture is represented in Fig. 20b. By introducing the aperture in the ground plane the field distribution changes, removing part of the field going from the strips of the top layer to the ground plane, and enhancing the fringing field between the two strips, hence making their coupling stronger. As usually done in couplers based on transmission line topologies the confronted area of the coupled lines it is a quarter wavelength at the central operating frequency.

Following this idea we have designed a pulse shaper that fits to the UWB mask, where the bandwidth of the frequency response is defined at -10 dB insertion losses. The material use for the design has a 0.508 mm thick substrate with dielectric permittivity of 3.38, with a 0.0027 loss tangent and the cooper on both sides has a thickness of 17 μm.

Fig. 21 shows the fabricated shaping network following the parallel coupled concept described above. The picture of the top layer with the two coupled transmission line reflects the compactness of the topology. The bottom layer includes the ground plane and the aperture used for enhancing the coupling strength between the two coupled lines.

The fabricated device has then been measured using a broadband network analyzer. Fig. 22a illustrates the shaping network frequency response from *DC* to 15 GHz. The frequency response is centered at 6.2 GHz and exhibit transmission zeros at *DC* and at 12.2 GHz. The results of the frequency response are then used to obtain the impulse response of the network. The results are depicted in Fig. 22. In this case the impulse response coincides with the intended output pulse since this network is proposed to be fed with a very narrow pulse.

(a) Top layer (b) Bottom layer. Dotted line is the top layer outline.

Fig. 20. Outline of the topology of the proposed shaping network.

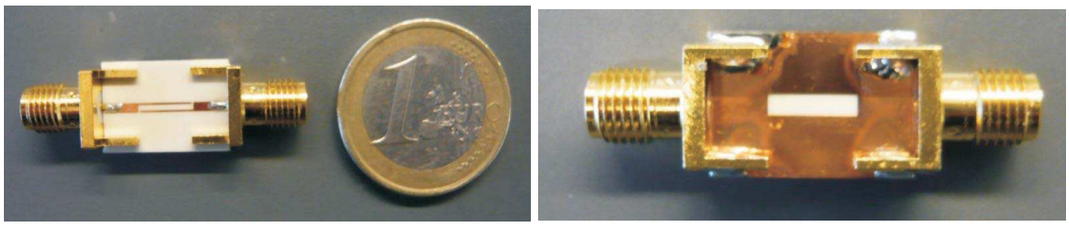

(a) Top layer (b) Bottom layer.

Fig. 21. Picture of fabricated shaping network.

Note as well, that such structure can be interpreted as a two order filter where the resonant frequencies are set by the length of the quarter wavelength transmission lines. Another interpretation would be a lumped series capacitor blocking the low frequency signals, where the cutting frequency at the lower band edge is set by the value capacitor (i.e; the coupling strength), and the open circuit quarter-wavelength stubs are producing a transmission zeros at twice of the central frequency.

6. Pulse Inverter/Non-Inverter

The pulse inverter is used in the present architecture (Fig. 23) because of the use of CDMA Direct Sequence Spread Spectrum. The key point of the inverter block lies in the transitions between balanced and unbalanced propagation modes. The pulse inversion is achieved by introducing a transition between unbalanced to balanced mode and, subsequently, a transition from balanced to unbalance but changing the reference plane at the output. This idea was introduced in (Gupta, 1996) using transitions between microstrip and coplanar slotlines.
The Inverter/Non-Inverter circuit has two different paths: one performs the pulse inversion whereas the other does not change the pulse sign. In Fig. 11 is depicted the final layout of this stage including the top and bottom layers. The Non-Inverter branch line has the same length as the Inverter branch. This is necessary to maintain both ways synchronized and same strip losses.

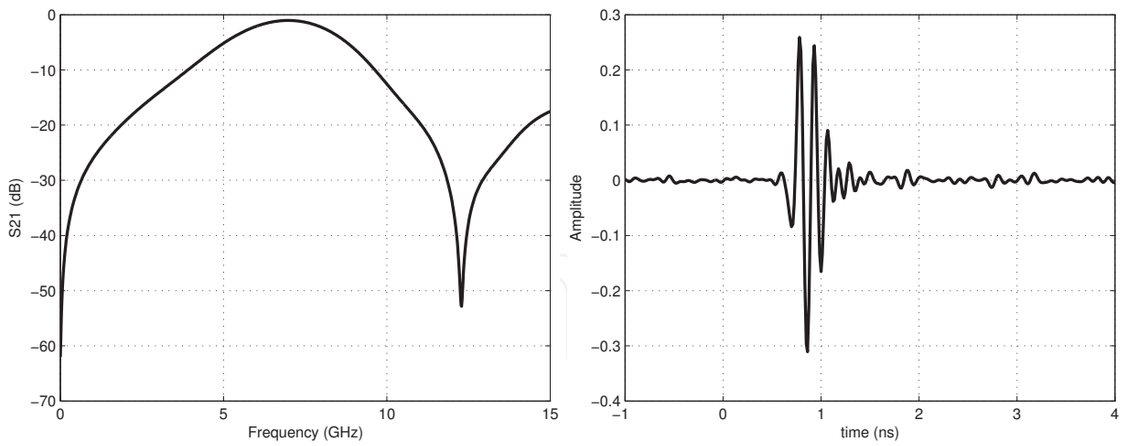

(a) Frequency domain. (b) Time domain.

Fig. 22. Measured time and frequency response of fabricated shaping network.

In Fig. 24 a measurement of the positive and negative pulses is depicted. The pulse width is 185ps, whereas the peak-to-peak amplitude is 2.2V. The generated pulses is caused by the inductive effect of the SRD package (Mollfulleda et al., 2006).

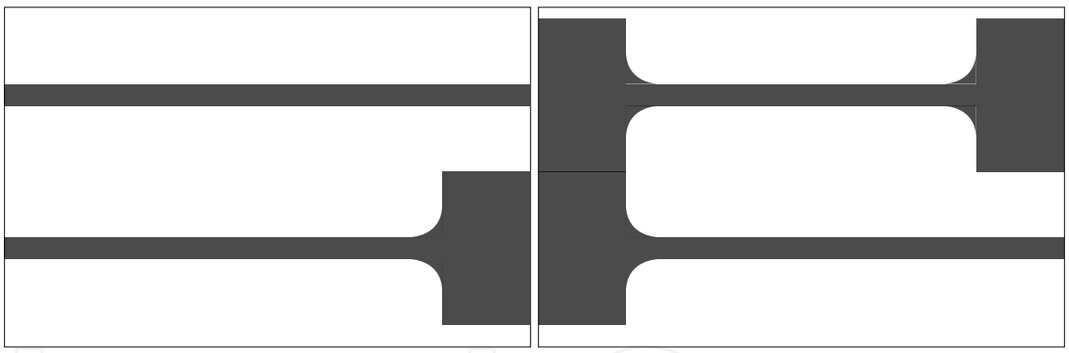

(a) Top Layer. (b) Bottom Layer. Dotted line represents the outline of the top layer

Fig. 23. Layout of implemented pulse inverter.

7. Power Combiner/Splitter

The power splitter/combiner is an essential device in both the transmitter and receiver chain (see Fig. 1). This section will present the design of a two-output/inputs power splitter/combiner. This design follows the concept of a coupled line configuration, where in the top-layer now three coupled lines are used to distribute the signal, whereas the required wide bandwidth performance is achieved by means of a coupling slot on the bottom layer.
To illustrate the functioning of the following approach, Fig. 25 shows the cross-section of a three coupled transmission lines, where in a power splitter case the line in the middle acts as a feeding strip, whose power is then distributed into the adjacent strips by means of fringing

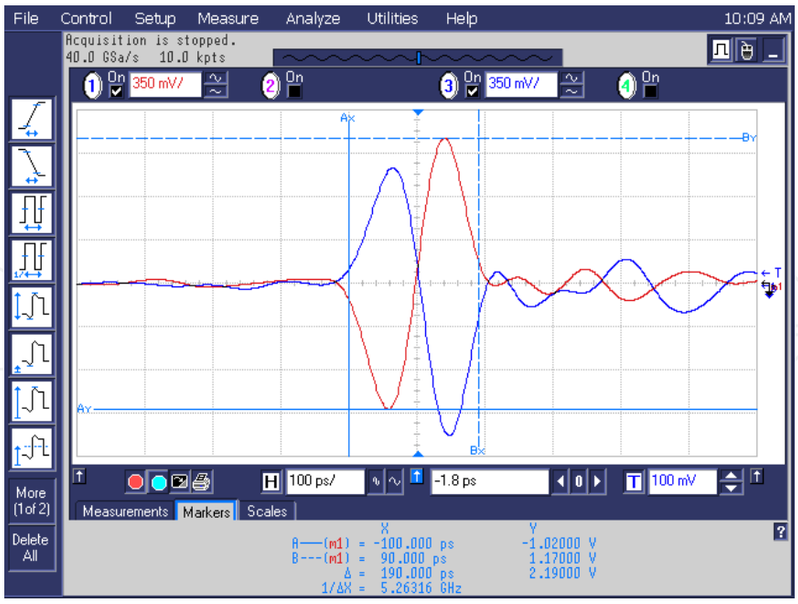

Fig. 24. Measurement of pulse inverted and non-inverted pulse.

field. In Fig. 25 we also outline the existing capacitances between the strips. In particular Fig. 25a outlines the capacitance between each strip and the ground plane (C_{ii}), and the capacitance between the strips C_{ij}. The capacitance between the strips set actually the strength of their couplings. As occurring in section 5.2 by removing the ground plane below the strips, the C_{ii} become negligible and the coupling between the strips (C_{ij}) increases, thus achieving a wider bandwidth response.

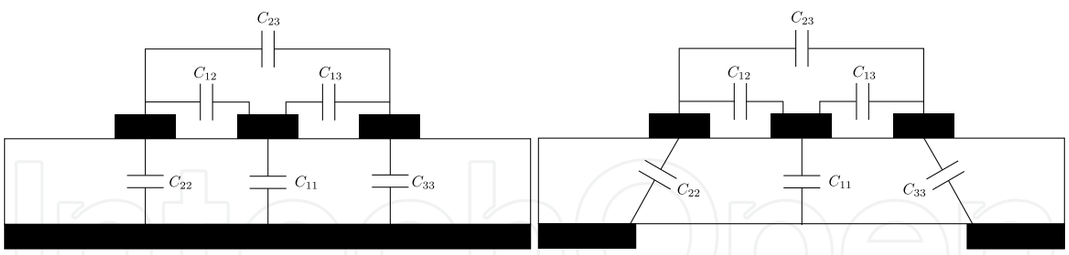

(a) Microstrip configuration. (b) Microstrip with apperture in ground plane

Fig. 25. Coss-section of a three coupled line structure.

Using this concept we have evaluated two topologies, which are outlined in Fig. 26. Both topologies have been designed in planar technology using a substrate with a dielectric permittivity of 3.38 and 0.508 mm of thickness, with 17 μm thickness of cooper metallization on both sides. Fig. 26a shows the topology of a wideband power splitter when no aperture exists in the ground plane, hence the equivalent circuit of an elemental section (i.e. the equivalent circuit of a cross-section), would correspond to the one of Fig. 25a. In order to improve the operation bandwidth we introduce an aperture slot in the ground plane (see Fig. 26b). By doing so the distributed capacitance on a cross-section of the three coupled lines follows the pattern outlined in Fig. 25b.

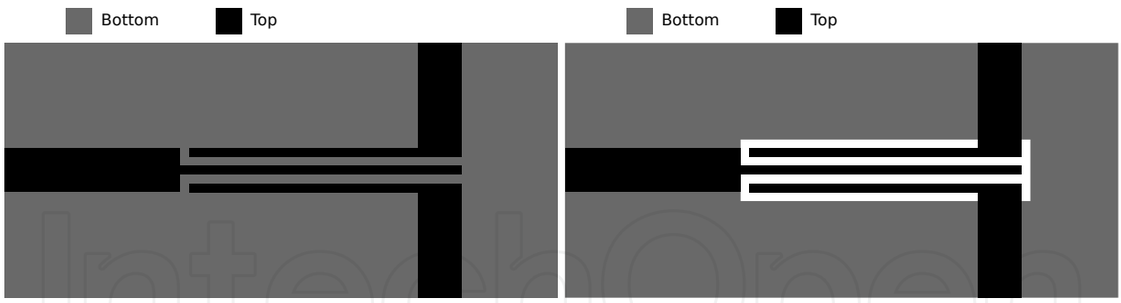

(a) Microstrip configuration. (b) Microstrip with apperture in ground plane

Fig. 26. Layout of power based on a three coupled line structure.

Both topology can be explained with the equivalent circuit model described in Fig. 27. This circuit model consists on a quarter-wavelength input transmission line modeling the center strip of the three coupled lines. The input strip is then coupled to two quarter-wavelength transmission lines, by means of two admittance inverters. These two lines are also coupled to each other by another admittance inverter. Being therefore this structure also interpreted as filtering structure with one input port and two output ports (diplexer), with identical response at both output ports.

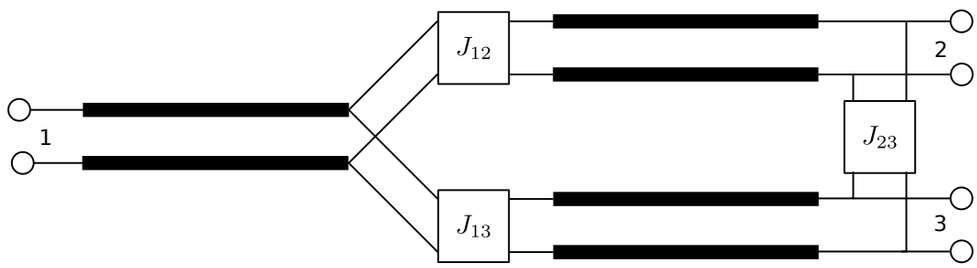

Fig. 27. Equivalent circuit topology of the proposed power splitter.

The designed power splitter of Fig. 26b had then been fabricated and measured. A picture of the top and bottom view of the fabricated devices is shown in Fig. 28a, where it can be observed the compactness of the design. The measured results of the transmission coefficient of the implemented filter are outlined in Fig. 28b, exhibiting the expected wideband response.

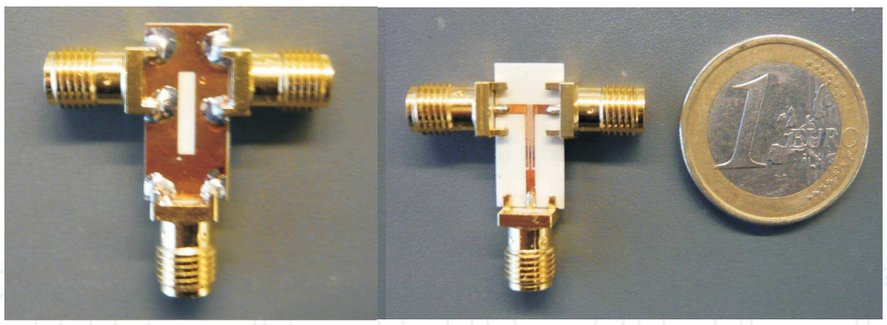

(a) Picture of implemented power splitter.

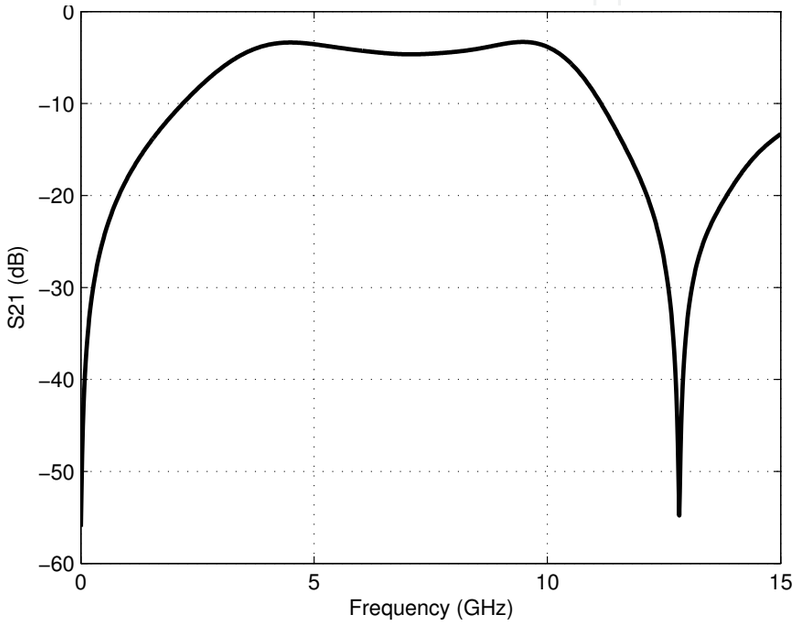

(b) Measured S21 of implemented power splitter

Fig. 28. Fabricated power splitter and measured response.

8. References

A., M., Najar, M., Miskovsky, P., Leyva, J. A., Berenguer, L., Ibars, C. & Navarro, M. (2006). Quetzal: Qualified ultra-wideband testbed for reduced data-rates and location, *IEEE International Conference on Testbeds and Research Infrastructures for the Development of Networks and Communities*, pp. 191–197.

Abbosh, A. M. (2007). Planar bandpass filters for ultra-wideband applications, *IEEE Trans. on Microwave Theory and Techniques* **55**(10): 2262–2269.

Barnes, M. A. (2000). *Ultra-Wideband Magnetic Antenna*, US Patent 6,091,374.

Bozzi, M., Pasian, M., Perregrini, L. & Wu, K. (2007). On the losses in substrate integrated waveguides, *Proceedings of 37th European Microw. Conf.*, Munich, pp. 384–387.

Burke, G. J. & Poggio, A. J. (1981). *Numerical Electromagnetics Code (NEC) - Method of Moments*, Rep. UCID18834, Lawrence Livermore Lab., Livermore, CA.

Chen, X., Drolet, D. & Wu, K. (2007). Substrate integrated waveguide filters for airborne and satellite system applications, *Proceedings of Canadian Conference on Eletrical and Computer Enginnering CCECE*, pp. 659–662.

Chuang, C., Lin, H. & Wang, C. (2007). Design of dual-mode siw cavity filters, *Proceedings of IEEE TENCON*, pp. 1–4.

Daubechies, I. (1990). The wavelet transform, time-frequency localization and signal analysis, *IEEE Trans. On Information Theory* **36**(5): 961–1005.

Deslandes, D. & Wu, K. (2001). Integrated microstrip and rectangular waveguide in planar form, *IEEE Microwave Wireless Comp. Lett.* **11**(2): 68–70.

Dissanayake, T. & Esselle, K. P. (2006). Correlation-based pattern stability analysis and a figure of merit for uwb antennas, *IEEE Trans. Antennas Propag.* **54**(11): 3184–3191.

EU (2007). 21 february 2007 - commission decision 2007/131/ec on allowing the use of the radio spectrum for equipment using ultra-wideband technology in a harmonised manner in the community, *Official Journal of the European Union* (L55): 33–36.

FCC (2002). Revision of part 15 of the commission's rules regarding ultra-wideband transmission systems, *Technical report*, Federal Communications Commission (FCC). `http://www.wireless.fcc.gov/rules.html`.

Guglielmi, M., Montauni, F., Pellegrini, L. & Arcioni, P. (1995). Implementing transmission zeros in inductive-window bandpass filters, *IEEE Trans. Microwave Theory Tech.* **43**(8): 1911–1915.

Gupta, K. C. (1996). *Microstrip Lines and Slotlines*, Artech House, Boston.

Hao, Z., Hong, W., Chen, J., Chen, X. & Wu, K. (2005). Compact super-wide bandpass substrate integrated waveguide (siw) filters, *IEEE Trans. Microwave Theory Tech.* **53**(9): 2968–2977.

Hong, H.-S. & Lancaster, M. J. (2001). *Microstrip Filters For RF/Microwave Applications*, John Wiley & Sons Inc.

Johnson, J. & Rahmat-Samii, Y. (1997). Genetic algorithms in engineering electromagnetic, *IEEE Antennas and Propagation Magazine* **39**(4): 7–21.

Kanda, M. (1978). A relatively short cylindrical broadband antenna with tapered resistive loading for picosecond pulse measurements, *IEEE Trans. Antennas Propag.* **26**(3): 369–373.

Li, K. (2006). Experimental study on uwb pulse generation using uwb bandpass filters, *IEEE International Conference on UltraWideband*, ICU, pp. 103–108.

Lindeblad, N. E. (1941). *Wideband Antenna*, US Patent 2,239,724.

Mira, F., Blas, A. S., Boria, V. & Gimeno, B. (2007). Fast and accurate analysis and design of substrate integrated waveguide (siw) filters, *Proceedings of 37th European Microw. Conf.*, Munich, pp. 170–173.

Mira, F., Mateu, J., Cogollos, S. & Boria, V. (2009). Design of ultra-wideband substrate integrated waveguide (siw) filters in zigzag topology, *IEEE Microwave Wireless Comp. Lett.* **19**(5): 281–283.

Miskovsky, P. (2010). *UWB antenna design for communication system performance optimization*, Ph.D. dissertation, Universitat Polytecnica de Catalunya-TSC.

Miskovsky, P., Arbesu, J. M. G. & Romeu, J. (2006). Application of uwb antenna descriptors to lossy dipole performance assessment, *Proceedings of IEEE Antennas Propag. Soc. Int. Symp.*, Albuquerque NM, pp. 175–178.

Miskovsky, P., Arbesu, J. M. G. & Romeu, J. (2007). What can we expect from a continuously tapered, resistivelay loaded monopole, for uwb applications, *Proceedings of IEEE Antennas Propag. Soc. Int. Symp.*, Honolulu HI, pp. 1421–1424.

Mollfulleda, A., Ibars, C. & Mateu, J. (2010). Ultra-wideband receiver based on microwave filterbbank, *IEEE International Conference on UltraWideband*, ICU.

Mollfulleda, A., Leyva, J. & Berenguer, L. (2006). Impulse radio transmitter using time hopping and direct sequence spread spectrum codes for uwb communications, *Proceeding of International Symposium on Advanced Radio Technologies, ISART*, NTIA, pp. 49–57.

Mollfulleda, A., Miskovsky, P. & J.Mateu (2005). Robust passive shaping network for impulse radio and uwb signal generator, *IEEE International Microwave Symposiumn*, pp. 1339–1342.

Montoya, T. P. & Smith, G. S. (1996). A study of pulse radiation from several broad-band loaded monopoles, *IEEE Trans. Antennas Propag.* **44**(8): 1172–1182.

Paulsen, L., West, J. B., Perger, W. F. & Kraus, J. (2003). Recent investigations on the volcano smoke antenna, *Proceedings of IEEE Antennas Propag. Soc. Int. Symp.*, vol. 3, pp. 845–848.

Rajo-Iglesias, E. & Quevedo-Teruel, O. (2007). Linear array synthesis using an ant-colony-optimization-based algorithm, *IEEE Antennas and Propagation Magazine* **49**(2): 70–79.

Rao, B., Ferris, J. & Zimmerian, W. (1969). Broadband characteristics of cylindrical antennas with exponentially tapered capacitive loading, *IEEE Trans. Antennas Propag.* **17**(2): 145–151.

Robinson, J. & Rahmat-Samii, Y. (2004). Particle swarm optimization in electromagnetics, *IEEE Trans. Antennas Propag.* **52**(2): 397–407.

Ross, G. (1965). The synthetic generation of phase coherent microwave signals for transient behaviour measurements, *IEEE Trans. on Microwave Theory and Techniques* **13**(5): 704–706.

Smith, P. W. (2002). *Transient Electronics, Pulsed Circuit Technology*, John Willey & Sons.

Tang, H., Hong, W., Chen, J., Luo, G. & Wu, K. (2007). Development of millimeter-wave planar diplexers based on complementary characters of dual-mode substrate integrated waveguide filters with circular and elliptic cavities, *IEEE Trans. Microwave Theory Tech.* **55**(4): 776–782.

Wu, T. T. & King, R. W. P. (1965). The cylindrical antenna with non-reflecting resistive loading, *IEEE Trans. Antennas Propag.* **13**(3): 369–373.

Zhang, Y., Hong, W., Wu, K., Chen, J. & Hao, Z. C. (2005). Development of compact bandpass filters with siw triangular cavities, *Proceedings of Asia-Pacific Micro. Conf. APMC*.

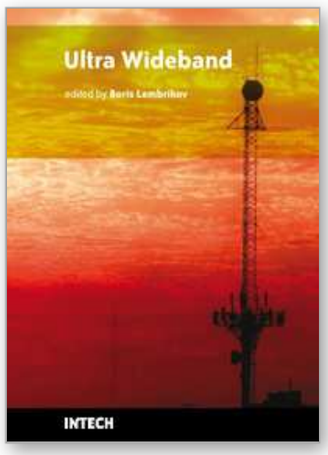

Ultra Wideband

Edited by Boris Lembrikov

ISBN 978-953-307-139-8
Hard cover, 458 pages
Publisher Sciyo
Published online 17, August, 2010
Published in print edition August, 2010

Ultra wideband technology is one of the most promising directions in the rapidly developing modern communications. Ultra wideband communication system applications include radars, wireless personal area networks, sensor networks, imaging systems and high precision positioning systems. Ultra wideband transmission is characterized by high data rate, availability of low-cost transceivers, low transmit power and low interference. The proposed book consisting of 19 chapters presents both the state-of-the-art and the latest achievements in ultra wideband communication system performance, design and components. The book is addressed to engineers and researchers who are interested in the wide range of topics related to ultra wideband communications.

How to reference

In order to correctly reference this scholarly work, feel free to copy and paste the following:

Fermin Mira Perez, Antonio Mollfulleda, Pavel Miskovsky, Jordi Mateu and Jose M. Gonzalez-Arbesu (2010). Passive Components for UWB Systems, Ultra Wideband, Boris Lembrikov (Ed.), ISBN: 978-953-307-139-8, InTech, Available from: http://www.intechopen.com/books/ultra-wideband/passive-components-for-uwb-systems

INTECH
open science | open minds

InTech Europe
University Campus STeP Ri
Slavka Krautzeka 83/A
51000 Rijeka, Croatia
Phone: +385 (51) 770 447
Fax: +385 (51) 686 166
www.intechopen.com

InTech China
Unit 405, Office Block, Hotel Equatorial Shanghai
No.65, Yan An Road (West), Shanghai, 200040, China
中国上海市延安西路65号上海国际贵都大饭店办公楼405单元
Phone: +86-21-62489820
Fax: +86-21-62489821

IntechOpen